JGR Space Physics

RESEARCH ARTICLE
10.1029/2019JA026720

# Seasonal Variations and Global Wave Distributions in the Mars Thermosphere From MAVEN and Multisatellites Accelerometer-Derived Mass Densities

**Jiandong Liu[1,2,3], Shuanggen Jin[1,2], and Yawen Li[1]**

[1]School of Remote Sensing and Geomatics Engineering, Nanjing University of Information Science and Technology, Nanjing, China, [2]Key Laboratory of Planetary Science, Shanghai Astronomical Observatory, Chinese Academy of Sciences, Shanghai, China, [3]University of Chinese Academy of Sciences, Beijing, China

**Key Points:**
- Diurnal cycles of the Mars thermospheric density are obtained and illustrated from multisatellite accelerometers
- Seasonal cycles of the Mars thermospheric density are investigated with linking both solar-heating and dust storms
- Coupling processes between internal atmospheric gravity waves (IAGWs) and dust activities are presented

**Correspondence to:**
S. Jin,
sgjin@shao.ac.cn;
sg.jin@yahoo.com

**Citation:**
Liu, J., Jin, S., & Li, Y. (2019). Seasonal variations and global wave distributions in the Mars thermosphere from MAVEN and multisatellites accelerometer-derived mass densities. *Journal Geophysical Research: Space Physics*, *124*, 9315–9334. https://doi.org/10.1029/2019JA026720

Received 12 MAR 2019
Accepted 28 SEP 2019
Accepted article online 17 OCT 2019
Published online 11 NOV 2019



**Abstract** Martian lower thermospheric variations are complex due to internal surface dust storms and external solar activities. However, limited Martian measurement data are restricted to observe and understand its variations in the past. In this paper, multisatellite accelerometer-derived densities and the Mars Climate Database are used to investigate seasonal variations, gravity waves, and coupling effects with the internal and external inputs, including *Mars Global Surveyor*, *Mars Reconnaissance Orbiter*, *Mars Odyssey*, and *Mars Atmosphere and Volatile EvolutioN Mission*. The diurnal and seasonal structures are reconstructed by the data, and the phase of the cycles is formed by solar heating/ionizing processes. Both amplitude and phase are impacted by surface dust activities during autumn and winter, for which density increases about 1.5–3.5 times compared to spring and summer seasons. A parameterized model that includes a newly introduced dust index is proposed to well fit and reinterpret the seasonal cycles. Furthermore, the coupling process between internal atmospheric gravity waves (*IAGWs*) and dust activities are investigated and explained. During dust storm times/seasons, the IAGWs exhibit both narrower amplitude peaks and deposit their energy at higher altitudes relative to "clear sky" times. The IAGWs could extend their energies into higher layers beyond exobase due to a thermospheric layer expansion (i.e., density increase) during dust seasons.

**Plain Language Summary** The new spacecraft *Mars Atmosphere and Volatile EvolutioN Mission* aims to observe Mars lower thermosphere from 100 to 200 km, namely, the lower thermosphere. The daily and yearly variations of the Mars thermospheric density are illustrated for the first time with this data. An improved fitting function is proposed for the yearly density variations. We found that the yearly variations are explained by seasonal solar illumination changes experienced by Mars during its orbit, which can be fit by a superposition of sine and cosine functions. The amplitude of the variations is impacted by surface dust storms during dust seasons (Mars northern autumn and winter). The behaviors of the vertically propagating internal atmospheric gravity waves (IAGWs) are investigated in different seasons. The interaction between these IAGWs and lower atmosphere dust storms is analogous to ocean waves hitting a beach, where the changes in the lower atmosphere dust function like the changing ocean depth close to shore that allow the ocean waves (i.e., IAGWs) to propagate more energy onto the shore (into the upper atmosphere).

## 1. Introduction

Studies of the Martian thermosphere can contribute to understanding atmospheric escape, investigating the evolution of Mars's climate, and assisting the search for exolife (e.g., Bougher, Cravens, et al., 2015; Di Achille & Hynek, 2010; Forget, 2013; Jakosky & Phillips, 2001; Jakosky, Lin, et al., 2015; Zurek et al., 2017). In order to achieve this scientific goal, thorough investigations into the structures and variations of the thermosphere are needed (e.g., Bougher, Cravens, et al., 2015; Jakosky, Lin, et al., 2015; Mahaffy et al., 2013). Multisatellite accelerometer (*ACC*)-derived densities obtained during the orbiter areobraking phase can provide key information about the Martian lower thermosphere (100–200 km). Previous investigations have suggested that the solar driving plays a central role in determining the state of the thermosphere, and this interpretation has been supported by observations made by the *Mars Atmosphere and Volatile EvolutioN Mission* (*MAVEN*) and by ground-based rovers (e.g., Bougher, Cravens, et al., 2015; Bougher, Jakosky, et al., 2015;

Bougher et al., 2017; Jakosky, Grebowsky, et al., 2015; Jakosky et al., 2017). In addition to solar forcing, other factors of the Martian atmosphere, such as surface dust distribution, atmospheric gravity waves, planetary waves, and global dynamics can also greatly impact the lower thermosphere (e.g., Bell et al., 2007; Keating et al., 1998; Rafkin et al., 2002; Wilson, 2002). Due to the lack of long-term and continuous data in the Martian thermosphere, isolating and investigating the different drivers are difficult. However, now with the MAVEN ACC density data, we can directly investigate the coupling mechanisms that have not been well characterized previously.

Early Mars missions such as Mariner 4/9 and Viking 1/2 used several sensors, including ACC, to derive densities and temperatures during the entry-descent-landing phase (e.g., Fjeldbo & Eshleman, 1968; Kliore et al., 1972; Nier & McElroy, 1977; Seiff & Kirk, 1977; Zurek & Leovy, 1981). These early ACC measurements at altitudes lower than 120 km limit their applicability to understand the full thermospheric density variations. From late 1990 to 2004, ACC-derived densities/temperatures and occultation profiles from the *Mars Global Surveyor* (*MGS*), *Mars Reconnaissance Orbiter* (*MRO*), *Mars Odyssey* (*ODY*), and *Mars Express* (*MEX*) missions played key roles in investigating the thermosphere (100–160 km; e.g., Bougher et al., 1999; Creasey, Forbes, & Hinson, 2006; Forbes et al., 2002; Forget et al., 2009; Keating et al., 2008; Liu et al., 2003; Tolson et al., 2005, 2007, 2008; Wang et al., 2006).

Various waves have been identified from the multitude of data sets obtained by these previous missions. Gravity waves were found to be ubiquitous below 100 km by the radio or stellar occultation profiles (e.g., Banfield et al., 2003, 2004; Creasey, Forbes, & Hinson, 2006). The upper atmosphere density variations were previously found to be dominated by Wave 2 and Wave 3 perturbations as indicated by the ACC densities (Keating et al., 2008). Moreover, Waves 4 to 6 signatures (*Rossby waves*) were also identified by a comprehensive analysis of the ACC-derived densities from MGS, ODY, and MRO, where the waves were observed in the thermosphere up to an altitude of 160 km (e.g., Forbes et al., 2002; Tolson et al., 2005, 2007; Wang et al., 2006). Horizontal and vertical wave-like structures were identified between 100 and 200 km from the MGS/MRO/ODY mass densities (e.g., Creasey, Forbes, & Keating, 2006; Fritts et al., 2006; Keating et al., 2008). However, due to the limited sampling at solar longitude (*Ls*) in previous data sets, the sources of these variations could not be sufficiently characterized and separated.

Previous work has identified several important phenomena in the thermosphere densities. First, the topographic thermal tide effects have been isolated in the MGS data (Withers et al., 2003). Additionally, Keating et al. (1998) demonstrated that the thermosphere mass densities show immediate responses to dust storms, where stationary planetary waves (i.e., Rossby waves) were thought to exist. Forbes et al. (2002) indicated that the perturbation likely represents diurnal Kelvin waves based on the Mars General Circulation Model (*MGCM*) simulations. Lastly, a thermosphere polar warming feature was identified from the MRO and ODY/ACC data sets (e.g., Bougher et al., 2006; Bell et al., 2007; González-Galindo, Forget, Lpez-Valverde, Angelats i Coll, & Millour, 2009; González-Galindo, Forget, Lpez-Valverde, & Angelats i Coll, 2009; Keating et al., 2008; Wilson, 2002). Despite these investigations, however, the global structure of these thermosphere density waves and their temporal evolution have not been fully characterized. Moreover,the diurnal and seasonal densities structure cannot be retrieved from the ACC densities.

The diurnal and seasonal cycle of the $CO_2$ density and temperature below 130 km can be illustrated by stellar occultation profiles of MEX (Forget et al., 2009), in which the harmonic structure of the cycles are not clearly compared with ACC-recovered cycles (Zurek et al., 2017). The occultation-deduced seasonal cycles are sensitive to dust activities, which might cause misconception that the lower thermosphere (100–200 km) is controlled by the dust storms. The precision of the occultation profiles is worse than the ACC-derived density data, and the numbers of the profiles are also limited. The combined MGS/MRO/ODY/MAVEN densities will contribute to describe the evolution of these cycles and gravity waves.

The MAVEN ACC-derived densities, owing to their unprecedented coverage in both space and time, enable the determination of the seasonal variations in the upper atmosphere. The annual density variations in the thermosphere are thought to be generated largely by solar radiation and winds, and these processes have been previously parameterized with two parameters, solar zenith angle (*SZA*) and Sun-Mars distance (Zurek et al., 2017). Additionally, the MAVEN Neutral Gas and Ion Mass Spectrometer (*NGIMS*) data have been used to investigate thermospheric gravity wave activities, and the vertical structures of the species from 120 to 260 km were described by Bougher, Cravens, et al. (2015), Bougher et al. (2017), and Yiğit et al. (2015).

Signatures of IAGWs have been detected in the main species densities of $CO_2$, Ar, and $N_2$ (e.g., England et al., 2016; 2017; Terada et al., 2017).

In this paper, we characterize the seasonal evolution of the thermospheric density and its force factors. The waves generated by the large-scale atmospheric dynamics are described and explained globally using seasonal mean (Ls = 90°) densities. The coupling between near-surface weather events, external solar activities, and thermospheric waves is investigated using a parameterized model. First, the open-accessed ACC-derived densities of the MGS/MRO/ODY and MAVEN are normalized into several reference altitudes with Laboratoire de Météorologie Dynamique Mars Climate Database (*LMD-MCD*). Second, the data are relocated with several indexes in terms of local solar time (LST), solar longitude (Ls), etc. In section 3, the data are either gridded (interpolated) or fitted (filtered) to analyze the variations. The principal components analysis (*PCA*, i.e., empirical orthogonal function, *EOF*) is implemented to extract the main components from the observations. The current parameterized model is improved to interpret the new data and phenomenon. The seasonal differences of the IAGWs and its reasons are investigated. The waves and their global distributions are presented. A brief discussion is given in section 4. Finally, conclusions are shown in section 5.

## 2. Materials and Methods

### 2.1. Data Processing

We use open access data sets (https://pds-atmospheres.nmsu.edu/data_and_services/atmospheres_data/MARS/mars_orbiter.html) of thermospheric mass densities derived from ACCs on board MGS, MRO, ODY, and MAVEN during the aerobraking phases. The process to derive the densities, its normalization referred to the LMD-MCD5.2, and the coverage of the observations are summarized below.

#### 2.1.1. Atmospheric Mass Density From ACC-Measured Acceleration

The retrieval of the atmospheric mass density from ACC-measured acceleration is based on the drag force formula. Commonly, the ACC measurements are mixtures of accelerations caused by conservative, nonconservative, calibrated, and noise forces (Tolson et al., 2008). The conservative terms are negligible due to the antigravity design of the ACC. The nonconservative accelerations are from effects of general relativity, solar radiation pressure, Martian radiation pressure (e.g., albedo and thermal inertia), and atmospheric drag effects $\mathbf{a}_{aero}$. The calibrated terms include perturbations triggered by ACC bias, thruster activities, and effects of angular motion of the ACC instruments with respect to the center of mass of the spacecraft (Zurek et al., 2015). The nondrag terms can be modeled, fixed, and then deducted from the measurements by using prior procedures in terms of navigational information, spacecraft records, and empirical models (e.g., Tolson et al., 2005, 2007, 2008). Subsequently, the aerodynamic acceleration $\mathbf{a}_{aero}$ is used to derive the atmospheric mass density as follows (e.g., Calabia & Jin, 2016; Tolson et al., 2005; Keating et al., 2008; Jin et al., 2018):

$$\mathbf{a}_{aero} = -\frac{1}{2}\rho C\frac{A}{m}|\mathbf{v}_{sc} - \mathbf{v}_{atmos}|^2\mathbf{e}_{rel} \tag{1}$$

where $\rho$ is the atmospheric mass density; $B = C \bullet A/m$ is the inverse ballistic coefficient; $m$ is the mass of the spacecraft; $A$ is the cross-sectional area perpendicular to the relative velocity direction $\mathbf{e}_{rel}$(unit vector); $C$ is the drag coefficient that approximates to 2.1 (Tolson et al., 2005); $\mathbf{v}_{sc}$ is the velocity of the spacecraft obtained from the Precise Orbital Determination (*POD*) products provided by Deep Space Network (*DSN*) navigation team; and $\mathbf{v}_{atmos}$ is the corotating velocity of the atmosphere along with Mars. The details of the formulation are found in Tolson et al. (2005, 2007, 2008).

#### 2.1.2. Density Normalization With Reference Model

Spacecraft is designed to aerobrake in the vicinity of the orbital periapsis to derive detectable aerodynamic acceleration $\mathbf{a}_{aero}$ from the ACC measurements as summarized in section 2.1.1. Aerobraking phases occur along a specific axis with respect to the body reference system, which stabilizes the state of the satellite to limit the calibrated terms such as attitude perturbations due to cross winds (Zurek et al., 2015). Consequently,the density is calculated only in the vicinity of the periapsis within ±300 s (inbound and outbound) in case of MAVEN. The data are arranged along the trajectories of the satellite.

The ACC measured mass density profiles obtained through aerobraking are normalized to several reference altitudes in order to investigate the spatial-temporal waves and variations. For lower Martian thermosphere

**Table 1**
*Ls Coverages of ACC-Derived Density* [a]

| Altitude(km) | MGS (MY23–MY24) | MRO (MY28, spring) | ODY (MY25, winter) | MAVEN (M32–MY34) |
|---|---|---|---|---|
| 100 | 85.8–90.1° | 51–99° | 280–301° | |
| 110 | 40–90°, 190–193° | 37–99° | 265–307° | |
| 120 | 34–95°, 183–299° | 36–99° | 263–307° | 10–196° |
| 130 | 34–95°, 183–300° | 36–99° | 262–307° | 10–196°, 290–330° |
| 140 | 34–95°, 183–300° | 36–99° | 261–307° | 10–196°, 290–330° |
| 150 | 34–95°, 183–300° | 34–99° | 261–307° | 7–330° |
| 160 | 34–95°, 183–300° | | | 0.5–356° |
| 170 | 34–95°, 183–300° | | | 0.5–356° |
| 180 | 34–95°, 183–300° | | | 0.5–356° |
| 190 | 183°, 234–287° | | | 0.5–356° |

*Note*. The surface dust storms evaluated by IR-CDOD during the missions are as follows: [*ODY* > *MGS* > *MAVEN* ≈ *MRO*]. The IR-CDOD data set can be downloaded and seen at http://www-mars.lmd.jussieu.fr/mars/dust_climatology/index.html during MY24 to MY33.
[a] Every 90° represents a season. For example, 0–90° is spring reference to the northern hemisphere.

from 100 to 200 km, there are two methods to regularize the data. As illustrated by Zurek et al. (2017), the data are projected into a reference altitude of 150 km by using density-scale height from atmospheric models. The projection will introduce model errors and variations into the original observations, which could distort and obscure variations due to gravity waves and thermal tides. Thus, this previous projection method is not suitable for studying the IAGWs and their effects. In this paper, we standardize the data into several reference altitudes of 10 km intervals in the vertical directions. The normalization equation is as follows (Calabia & Jin, 2016):

$$\rho(\lambda, \phi, z_{ref}, t) = \rho(\lambda, \phi, z, t)\frac{\rho_{mcd}(\lambda, \phi, z_{ref}, t)}{\rho_{mcd}(\lambda, \phi, z, t)} \tag{2}$$

where $\lambda$ is longitude; $\phi$ is areolatitude; $z$ represents altitude where the measurements were carried out; and $z_{ref}$ represents reference altitude, where $|z_{ref} - z| \leq 5$ km. Consequently, $\rho(z)$ is density measurement; $\rho(z_{ref})$ is normalized density. Correspondingly, $\rho_{mcd}(z)$ is model density at measurements altitude $z$; $\rho_{mcd}(z_{ref})$ is model density at reference altitude $z_{ref}$. We use LMD-MCD, Version 5.2, as a reference model to normalize the data. The LMD-MCD5.2 database is an assimilated data set where the data are simulated results of MGCM under comprehensive scenarios (Angelats i Coll et al., 2005; González-Galindo, Forget, Lpez-Valverde, Angelats i Coll, & Millour, 2009; González-Galindo, Forget, Lpez-Valverde, & Angelats i Coll, 2009). In order to maintain consistency between the measurements and the MCD, the scenarios that reflect the surface dust and solar activities should be set properly based on Millour et al. (2015) and Montabone et al. (2015).

### 2.1.3. Density Coverages

The density coverages are summarized in Tables 1 and 2. The MGS observed the first density profile at Ls 183°, Mars Year (MY23) during the autumn-winter global dust seasons. The densities cover Ls 180–300° from altitude 110 to 180 km (Table 1, MGS), when the observations have a distinct response to the dust impact (Keating et al., 1998). The MGS observations extends to the beginning of the summer (Ls 95°), MY24. Most of the MY24 spring months (2 and 3) are covered when the dust activities are more active compared with other MYs. Most of the mass density observations occur between 120 and 170 km altitude. The start time of MRO densities is Ls 34.7°, MY28, and the stop time is Ls 99°, MY28 (Table 1, MRO). MY28 spring is clear of dust. The densities vertical coverage is mainly limited to 120–150 km with few observations located at 100–110 km. The ODY densities start at Ls 261° and stop at Ls 300°, MY25. The MY25 autumn and winter were experiencing typical global dust storms. MAVEN densities start at Ls 209°, MY32. The dust loading of Ls 209–280° (MY32) is lower than the MY24 autumn-winter season. The dust storms of Ls 280–360° (MY32) are higher than in MY24 winter. The dust loading of MY33 is lower than in MY24. The densities stop at Ls 174° MY34 (this paper). The dust loading is evaluated by *Infrared Column Dust Optical Depth* (*IR-CDOD*) (Montabone et al., 2015; Smith, 2009).

Journal of Geophysical Research: Space Physics

10.1029/2019JA026720

**Table 2**
*Global Coverages of ACC-Derived Density*[a]

| | | Spring (0°<Ls<90°) | | Summer (90°<Ls<180°) | | Autumn (180°<Ls<270°) | | Winter(270°<Ls<360°) | |
|---|---|---|---|---|---|---|---|---|---|
| Altitude(km) | d$\rho$/$\rho$×100% | Day | Night | Day | Night | Day | Night | Day | night |
| 100 | 2.67% | 63.8°S to 86.5°S | 63.1°S to 87.1°S | | 13°S to 85.8°S | | | | 86.3°N to 64.5°N |
| 110 | 2.84% | 53.8°N to 86.5°S | 59.2°S to 87.1°S | 82.9°S to 86.5°S | 7.5°N to 87.1°S | 37.7°N to 28.2°N | 75.7°N to 64.7°N | | 86.3°N to 16.2°N |
| 120 | 4.19% | 62.1°N to 86.5°S | 56.7°S to 87.1°S | 77.5°S to 86.5°S | 40.9°N to 87.2°S | 52.6°N to 24.8°N | 78.7°N to 9.3°S | 65.3°N to 42.6°N | 86.3°N to 2.5°N |
| 130 | 6.08% | 66.5°N to 86.5°S | 22°N to 87.1°S | 73.2°S to 86.7°S | 44.1°N to 87.2°S | 56°N to 22.5°N | 80.8°N to 13.4°S | 68.2°N to 10.9°S | 86.3°N to 5.3°S |
| 140 | 6.53% | 68°N to 86.5°S | 26.1°N to 87.1°S | 69.6°S to 86.6°S | 47.9°N to 87.2°S | 58.2°N to 20.9°N | 82.5°N to 16.2°S | 70.3°N to 14.7°S | 86.3°N to 10.9°S |
| 150 | 13.60% | 69.9°N to 86.5°S | 72.7°N to 87°S | 48.5°S to 86.5°S | 67.3°N to 87°S | 74.1°N to 20.6°N | 83.9°N to 33.3°S | 72.1°N to 17.2°S | 86.4°N to 50.8°S |
| 160 | 30.20% | 71.5°N to 73.1°S | 74.4°N to 74.3°S | 74.4°N to 82.3°S | 73.8°N to 5.8°N | 74.3°N to 50.5°S | 74.4°N to 50.4°S | 73.4°N to 38°S | 72.4°N to 66.1°S |
| 170 | 41.80% | 72.6°N to 73.3°S | 74.4°N to 74.3°S | 74.4°N to 43.4°N | 74.1°N to 3.5°N | 74.3°N to 55.7°S | 74.4°N to 53°S | 74°N to 74.3°S | 73.3°N to 72.9°S |
| 180 | 75.70% | 70.9°N to 73.3°S | 74.4°N to 74.3°S | 74.4°N to 41°N | 74.2°N to 1.5°N | 74.4°N to 74.3°S | 74.4°N to 55.8°S | 56.7°N to 74.3°S | 73.9°N to 73.6°S |
| 190 | 167.80% | 70.6°N to 73.1°S | 74.4°N to 74.3°S | 74.4°N to 39.1°N | 74.3°N to 0.3°S | 74.4°N to 74.1°S | 74.4°N to 57.1°S | 50.9°N to 74.3°S | 74.3°N to 73.9°S |

*Note.* The average IR-CDOD (Pa/Pa) values for different seasons are as follows: Spring (0.075–0.15); summer (<0.075); autumn (0.225–1.0); winter (0.225–0.525). The mean density (kg/km$^3$) in different latitudes (near equatorial region[1], midlatitude of NH[2] and SH[3], north polar region[4], and south polar region[5]) at altitude of 160 km in dayside is as follows: spring ($0.1^1$, $0.35^2$, $0.25^3$, $0.35^4$, $0.05^5$); summer ($0.35^2$, $0.35^4$, $0.05^5$); autumn ($0.05^1$, $0.4^2$, $0.4^3$, $0.05^4$, $0.4^5$); winter ($0.18^1$, $0.07^2$, $0.07^3$, $0.05^4$, $0.4^5$).
The data altitude higher than 150 km are mainly from MGS and MAVEN, especially the latter.

**Table 3**
*Nonmigrating Wave Interactions (Forbes et al., 2002)*[a]

| Migrating solar radiation frequency component, or tide frequency component ($n$) | Topographic wave number, stationary wave number Sun-synchromous wave number ($m, k_s$) | Planetary wave number $n+m$ | $s$ $n-m$ |
|---|---|---|---|
| 1 | 1 | 2 | 0 |
| 1 | 2 | 3 | -1 |
| 1 | 3 | 4 | -2 |
| 2 | 1 | 3 | 1 |
| 2 | 2 | 4 | 0 |
| 2 | 3 | 5 | -1 |

[a] The Mars topography has a typical $m = 2$ wave number.

As seen in Tables 1 and 2, current observations provide good global coverage at altitude 150–170 km with ratio of derived error/density less than 42%, which is shown in Table 2. The data have good coverage at spring (dayside) and winter with altitude higher than 150 km. The paper mainly uses densities at 160 km to investigate the variations and cycles. Other observations in different altitude are used to verify and validate the results. For the solar activities, the MGS and ODY missions are located in the solar maximum cycles (1999–2002). The MRO is at solar minimum (2006). The MAVEN experiences the solar maximum cycles (2014–2016) again, but the amplitude is lower than the former one, which can be evaluated by $F_{10.7}$ index (Earth). The year 2017–2019 is solar minimum again. The solar $F_{10.7}$ can be obtained online from https://omniweb.gsfc.nasa.gov/form/dx1.html.

## 2.2. Analysis Methods

### 2.2.1. Variations and Waves From PCA

The measured mass densities are projected to a set of reference altitudes according to equation (2), and these projected densities can then be organized by key parameters, such as LST, geographic longitude, or another geophysical parameter. Then, the densities can be gridded and interpolated along this parameter space to generate a matrix, for example, $P_{m\times n}$. Each row represents a snapshot at a fixed time, while each column represents the time evolution at a fixed point in parameter space. PCA (also called EOFs) is employed to isolate and extract the dominant spatial and temporal variations present in the ACC mass density data at a fixed altitude. The PCAs or EOFs of the $P$ are the principal (uncorrelated) components of the matrix determined by transformation $RC = C\Lambda$ (Abdi & Williams, 2010; Calabia & Jin, 2016). Technically, the calculation is as follows: The covariance matrix is $R = P^T P$; second, the eigenvalues and eigenvector can be extracted from $R_{n\times n}$ by the transformation. The $\Lambda$ is a diagonal matrix where the diagonal elements $\lambda_i$ are eigenvalues of the $R$; each column $\alpha_i$ of $C_{n\times n}$ is the eigenvector of $R$, which is the principal component of the map, that is, $EOF_i = \alpha_i$ or $EOF_i = \alpha_i/|\alpha_i|$. Additionally, the data explained by the components are equal to the percentage of the corresponding eigenvalue in the sum of all eigenvalues (explained $= |\lambda_i|/\sum_{j=1}^{n}|\lambda_i|$), where absolute values are used. The components are also centralized (labeled as *c-EOF* or *c-PCA* in this paper ), in which the c-PCAs or c-EOFs are between −1 and +1. The PCA method is capable of identifying several uncorrelated variables to represent the original data (Abdi & Williams, 2010).

### 2.2.2. Wave Interaction and Recognition

The harmonics generated by the periodic absorption of energies from solar irradiation and surface topography during the rotation of Mars can be represented by subharmonics of its rotational period, $T$. The responses in the atmospheric parameters $\xi$ can be illustrated by sum of harmonics as follows (Forbes et al., 2002; Fritts et al., 2006):

$$f(\xi) = \sum_n \sum_s A_{n,s}(z,\phi)\cos[n\Omega t + s\lambda - \varphi_{n,s}(z,\phi)] \tag{3}$$

where $t$ is time in sols; $s$ is zonal wave number; $\Omega = 2\pi/\text{sol}$ is the planetary rotation rate; $A_{n,s}$ is the amplitude; $\varphi_{n,s}$ is the phase (maximum at latitude $\lambda = 0°$); $n = 1, 2, \ldots$ represents diurnal (D), semidiurnal tide (S), etc.

Equation (3) represents a series of zonally propagating waves with phase speeds equal to $-n\Omega/s$, in which the $\pm$ of $s$ implies the propagation directions ($s > 0$ is westward (W) propagating waves and vice versa (E)). Rewriting in terms of LST by $t = t_{LST} - \lambda/2\pi$, equation (3) is as follows:

$$f(\xi) = \sum_n \sum_s A_{n,s}(z,\phi)\cos[n\Omega t_{LST} + (s-n)\lambda - \varphi_{n,s}(z,\phi)] \quad (4)$$

Zonal wave number caused by the components of surface topography is denoted by $m$. The oscillations can be represented by sum of harmonics as $\sum \cos(m\lambda - \varphi_m)$. The superposition of (3) and (4) with topographic waves generates complex variations in Martian thermosphere, as discussed by Forbes et al. (2002) and summarized in Table 3.

## 3. Results and Analysis

### 3.1. Diurnal and Seasonal Cycles

#### 3.1.1. Diurnal Cycles

Previously, diurnal signatures in the Martian thermosphere mass densities could not be isolated. However, the density coverage provided by MAVEN enables the extraction of diurnal cycles in all seasons from altitude 160 to 190 km. The LST of the cycles are not completely covered in all seasons below altitude 160 km or higher than 190 km by the densities. We use the altitude of 160 km to describe the cycles: (1) to minimize the ACC-derived errors, (2) to isolate both the internal and external variables that have distinct effects on this altitude as illustrated in sections 3.1.2 and 3.2, and (3) to make use of the better data coverage at this altitude as shown in Tables 1 and 2. In those tables, and throughout this paper, seasons are defined relative to the northern hemisphere (*NH*) using Ls.

The density diurnal cycles of all seasons are shown in Figure 1. The spring (Ls = 0–90°) cycle is a two-trough structure. The cycle experiences dayside (LST 6–18 hr) increase and reaches its peak (0.03 kg/km$^3$ < $\rho$ < 0.1 kg/km$^3$) at LST 12–15 hr. The increase is due to solar heating/ionizing. The first trough appears at about 21 hr, where the density can be less than 0.02 kg/km$^3$. The second trough occurs at 4:30 hr in the next-day morning. Thus, another small peak exists in the midnight, where the density is as high as 0.05 kg/km$^{-3}$. The derived errors are less than 0.05 kg/km$^{-3}$ except the outliers between LST 14 and 17 hr. The cycle can be fit by a four-stage *Fourier series* (*FS*) with 95% predicted bounds. The coefficients are in Table 4. The outliers between 14 and 17 hr have been ignored during the fitting due to the revulsions of the derived errors. The summer diurnal cycle has a single peak (earlier than noon), in which the amplitude and day-night difference are larger than the spring counterpart. The summer densities are mostly from MAVEN (MY33) where dust storms are absent (Montabone et al., 2015). The summer diurnal cycle exhibits a fast morning increase but slow afternoon decline. The trough of the structure is displayed at LST 3 hr in the next-day morning. The autumn diurnal cycle has a distinct afternoon peak (LST = 15 hr), where the densities slowly rise to a daily maximum and then rapidly drop during the night, exhibiting the strongest diurnal density cycle amplitude among the four seasons. These trends are likely explained by the autumn slow absorption of solar radiation (heating) during the day, followed by comparatively rapid cooling processes during the night. The amplitude, which reaches around 0.3–0.5 kg/km$^{-3}$, is nearly doubled compared to other seasons. It is an impact generated by surface dust activities which is first detected by MGS data (Keating et al., 1998). The atmosphere density drops down after the crest (LST = 15 hr) within 6 hr. The trough is around midnight. The winter structure cannot be illustrated completely by observations at altitude 160 km due to lack of data in LST 3–8 hr. However, the cycle still can be recovered by harmonic fitting. It is also a single-peak structure that is symmetric to the LST = 12 hr.

The MCD counterparts of the diurnal cycles are illustrated in Figure 2. The spring night density irregularities are reflected, or even overestimated. The cycle is modeled by nonlinear interaction (the $n$ will not be an integral) of diurnal ($n = 1$) and semidiurnal ($n = 2$) tides. The orographic terms are added into the model with $m = 2$ wavenumber. The model structures are consistent with observations but exhibit some slight phase differences. The summer diurnal cycle can be modeled by harmonics with diurnal wavenumber $n = 1$ solely. It has phase differences with the measurements. The cycle experiences fast heating and slow cooling processes due to intense thermal absorption and extended radiative cooling. The summer cycle is well represented by the MCD. The autumn cycle model is similar to the spring. The nightside densities are overestimated by the MCD. The dust scenario is used based on MY24 dust IR-CDOD. For winter, the cycle is modeled by diurnal tides. The diurnal cycle is similar to the spring structure. The time spent by the energy absorption and release process is the same as deduced from Figure 2. The crest is at LST 12 hr. The trough is at midnight. The MCD values are overestimated at night.

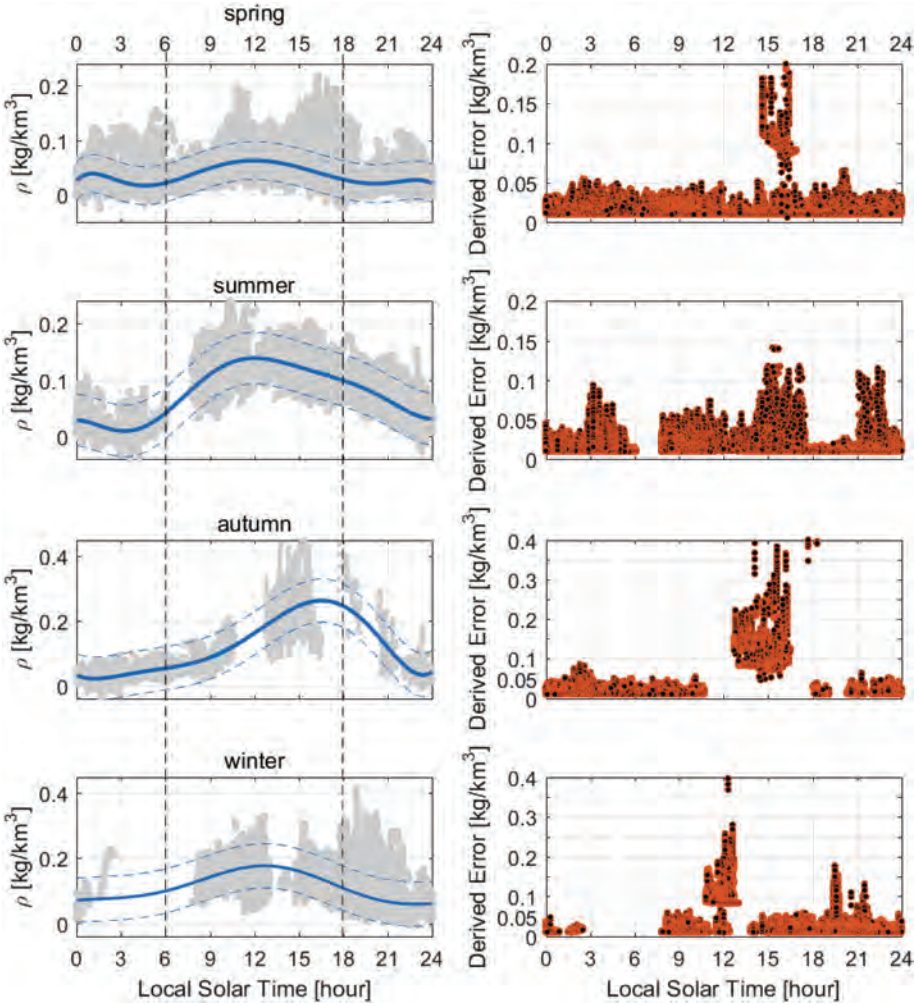


**Figure 1.** Seasonal differences of diurnal cycle at altitude of 160 km. (left) ACC-derived densities. Solid blue line: harmonics fitting with 95% predicted bounds (dash blue line). The coefficients are show in Table 4. (right) derived errors. The error-observation ratio is about 30–50%. The ratio more than 50% at certain LST is caused by nonconvergent value when using iterative algorithm to solve equation (1) (Tolson et al., 2005) or dust impacts. By fitting the cycles with harmonics, a seasonal amplitude and phase evolution are found.

A seasonal evolution of the diurnal cycles can be observed by data interpolation and its PCAs (Figure 3). PCA1 represents the diurnal cycle, as revealed by the observations. Thus, the seasonal evolution of PCA1 should reflect the seasonal changes in the diurnal cycles. Other cycles such as semidiurnal variations are not clear due to the lower explained percent (< 3%) (PCA2–PCA6).

The latitude differences of the diurnal cycles are shown in Figure 4. The measurement coverage is not good, but the main features still can be seen. The MAVEN ACC densities confirm the seasonal latitude trends that have partially pointed out in both data and modeling studies (e.g., Creasey, Forbes, & Hinson, 2006; Creasey, Forbes, & Keating, 2006; Fritts et al., 2006). *GCM* simulation is also performed to verify the results. A quick overview of the results is as follows: The spring has a higher density in the NH compared to the southern hemisphere (SH). The summer season lacks data coverage in the SH. Therefore, the summer diurnal cycle in Figure 1 is the NH midlatitude variations. The autumn has higher density in the midlatitude and a cold equatorial region. The winter equatorial warming is detected, which is not predicted by the GCM. For the other three seasons, latitude variations can be simulated by the GCM. The seasonal evolution of the diurnal cycles is also found.

Overall, a seasonal evolution of the Mars thermospheric diurnal cycles is reflected by the ACC-derived densities. The diurnal phase evolution is due to the orbit evolution of Mars along the Sun (Zurek et al., 2017),

**Table 4**
*Coefficients of the Diurnal-Seasonal Harmonic Fitting*

| FS | | $f(LST) = a_0 + \sum_{i=1}^{k} a_i \cos(w \cdot LST) + \sum_{j=1}^{k} b_j \cos(w \cdot LST)$ | | |
|---|---|---|---|---|
| Diurnal | | Coefficients | Confident bounds(95%) | Fitting goodness |
| Spring | a0 | 0.03048 | (0.02732, 0.03364) | |
| | a1 | 0.02223 | (0.01718, 0.02728) | |
| | b1 | 0.003152 | (0.002798, 0.003506) | |
| | a2 | 0.002754 | (−0.001732, 0.00724) | SSE: 36.26 |
| | b2 | 0.005907 | (0.004725, 0.007088) | *R*-square: 0.3872 |
| | a3 | 0.01076 | (0.007191, 0.01432) | Adjusted *R*-square: 0.3872 |
| | b3 | 0.003418 | (0.001741, 0.005095) | RMSE: 0.01922 |
| | a4 | −0.005792 | (−0.0067, −0.004884) | |
| | b4 | −0.003473 | (−0.00409, −0.002856) | |
| | w | 1.084 | (1.045, 1.123) | |
| Summer | a0 | −4,457 | (−7.073e+04, 6.181e+04) | |
| | a1 | 7,141 | (−9.895e+04, 1.132e+05) | |
| | b1 | 501.4 | (−6,148, 7,151) | |
| | a2 | −3,583 | (−5.67e+04, 4.954e+04) | SSE: 30.05 |
| | b2 | −509.9 | (−7,237, 6,217) | *R*-square: 0.4175 |
| | a3 | 1,027 | (−1.417e+04, 1.622e+04) | Adjusted *R*-square: 0.4175 |
| | b3 | 224.6 | (−2,713, 3,162) | RMSE: 0.0177 |
| | a4 | −128.4 | (−2,026, 1,769) | |
| | b4 | −38.83 | (−541.1, 463.4) | |
| | w | 0.218 | (−0.1977, 0.6337) | |
| Autumn | a0 | 65.8 | (−31.02, 162.6) | |
| | a1 | −100.8 | (−248.3, 46.79) | |
| | b1 | −12.64 | (−27.25, 1.965) | SSE: 53.15 |
| | a2 | 43.21 | (−18.71, 105.1) | *R*-square: 0.7506 |
| | b2 | 10.69 | (−1.254, 22.64) | Adjusted *R*-square: 0.7506 |
| | a3 | −8.169 | (−19.37, 3.032) | RMSE: 0.03406 |
| | b3 | −2.825 | (−5.899, 0.2483) | |
| | W | 0.509 | (0.3897, 0.6284) | |
| Winter | a0 | 0.09952 | (0.09531, 0.1037) | |
| | a1 | 0.02113 | (0.01678, 0.02548) | SSE: 196.1 |
| | b1 | −0.05038 | (−0.05157, −0.04919) | *R*-square: 0.3468 |
| | a2 | 0.004106 | (0.003367, 0.004845) | Adjusted *R*-square: 0.3468 |
| | b2 | −0.008475 | (−0.01129, −0.005658) | RMSE: 0.04379 |
| | w | 0.8529 | (0.7879, 0.9178) | |
| FS | | $f(Ls) = a_0 + \sum_{i=1}^{k} a_i \cos(w \cdot Ls) + \sum_{j=1}^{k} b_j \cos(w \cdot Ls)$ | | |
| Seasonal | a0 | 0.07573 | (0.07557, 0.07589) | |
| | a1 | −0.01033 | (−0.01057, −0.01009) | |
| | b1 | 0.02694 | (0.02671, 0.02716) | |
| | a2 | 0.005657 | (0.005434, 0.005879) | |
| | b2 | −0.01317 | (−0.01341, −0.01293) | |
| | a3 | −0.02134 | (−0.0216, −0.02108) | |
| | b3 | 0.004284 | (0.004036, 0.004533) | |
| | a4 | −0.02223 | (−0.02246, −0.022) | SSE: 470.5 |
| | b4 | −0.0396 | (−0.03983, −0.03936) | *R*-square: 0.517 |
| | a5 | −0.0161 | (−0.01635, −0.01586) | Adjusted *R*-square: 0.517 |

**Table 4** *continued*

| FS | | $f(LST) = a_0 + \sum_{i=1}^{k} a_i \cos(w \cdot LST) + \sum_{j=1}^{k} b_j \cos(w \cdot LST)$ | | |
|---|---|---|---|---|
| Diurnal | | Coefficients | Confident bounds(95%) | Fitting goodness |
| | b5 | −0.01008 | (−0.01037, −0.009796) | RMSE: 0.0375 |
| | a6 | 0.01075 | (0.0105, 0.011) | |
| | b6 | −0.005869 | (−0.006092, −0.005645) | |
| | a7 | −0.0005631 | (−0.0008357, −0.0002904) | |
| | b7 | 0.0127 | (0.01246, 0.01295) | |
| | a8 | −0.0001955 | (−0.0004297, 3.87e−05) | |
| | b8 | 0.003867 | (0.003573, 0.004161) | |
| | w | 1.901 | (1.898, 1.904) | |

*Note*. LST = 0–24 hr. *Ls* = 0–360°. All data are used.

which can be validated by the rover's surface temperature data and GCM simulation (Forget et al., 2009). The amplitude evolution is related to the surface dust storms. The thermospheric mass densities are nearly doubled during the dust seasons (Ls 135–360°). The seasonal evolution will be completely explained in section 3.1.2.

### 3.1.2. Seasonal Variations Forced by Solar Heating and Dust Storms

The structure of the Martian thermosphere has been believed to be controlled by the orbital obliquity evolution of Mars around the Sun as well as the radiation and winds from the Sun (Bougher, Cravens,et al., 2015; Bougher, Jakosky, et al., 2015; Bougher et al., 2017). The seasonal cycles of $CO_2$ density variations of the Martian upper atmosphere are firstly described by MEX stellar occultation data and verified with MGCM (Forget et al., 2009). The data have limited resolution to describe the harmonic variation of the cycles at a fixed altitude. The cycles illustrated by the ACC data, synonymously, atmospheric mass density, are unavailable for seasonal variation prior to the observations from MAVEN. The seasonal variation described by the MAVEN ACC-derived density is firstly investigated by Zurek et al. (2017), in which the variation is parametrized with SZA and Sun-Mars distance. The seasonal evolution is also reflected in Figures 1–4. However, the diurnal cycles summarized in section 3.1.1 have seasonal amplitude differences and density irregularities from spacecraft to spacecraft. The differences indicate that there are other factors besides solar radiation that could influence the thermosphere from 100–200 km.

The annual pattern of the Martian thermospheric density at altitude of 160 km is shown in Figures 5 and 6. Each of the season except winter has a single density peak (Figure 6a). The autumn density has a distinct peak that can be clearly reflected in both longitude and latitude directions (Figures 5a and 5c). The autumn is the most dusty season of the whole year as evaluated by the IR-CDOD index (Figures 5b and 5d), which could influence the thermosphere by large-scale dynamics or dust radiation. The thermospheric density responses to the autumn dust is firstly captured by MGS data (Keating et al., 1998).

The seasonal longitude variation is shown in Figures 5e–5h. There is a trough existing between the double peaks of the winter, which is due to the impact of the "re-expand" of surface dust storms (Figure 5e). The autumn amplitude reaches the annual maximum. The winter amplitude is a little larger than the summer. The spring peak is the annual minimum especially during nightside (Figure 5h). It coincides with the seasonal evolution of the diurnal results in section 3.1.1.

The seasonal density time series are shown in Figure 6. Both dayside and nightside data have harmonic structure(Figures 6b and 6c). The annual cycle is well recovered by the MCD simulation (Figures 6e, 6f, and 6g), in which the harmonic variation is not perfect compared to the observations. Except for summer, the surface dust storms represented by IR-CDOD are correlated with the annual thermospheric density variation especially in dust seasons (Figure 6d). The coincidences are also reflected by the PCA1 (IR-CDOD) and *EOF1* (density) as shown in Figure 6h.

The annual harmonic density cycle was thought to be caused by the obliquitous evolution of the Mars along the Sun that the solar fluxes vary with respect to the orbit elements, which can be parametrized by SZA,

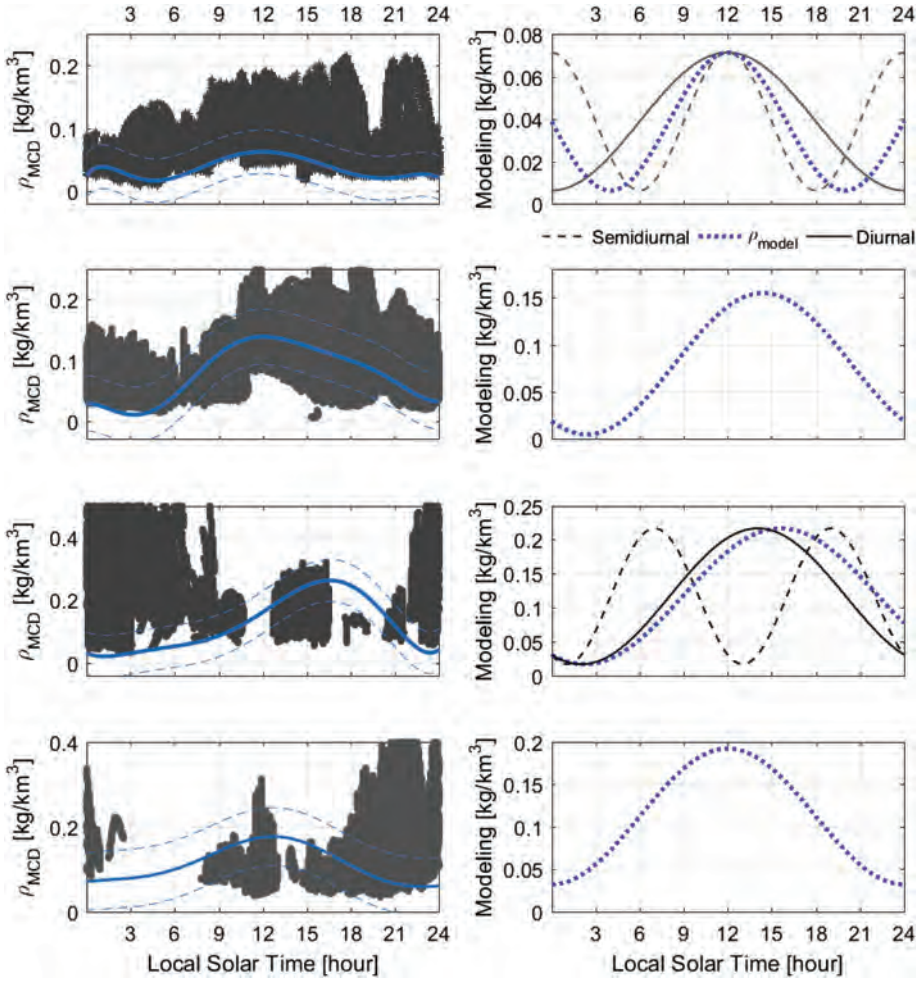


**Figure 2.** (left) densities from MCD model. The solid and dashed blue lines are the observation fitting and 95% predicted bounds from Figure 1. (right) Modeling based on equation (4). The night amplitudes are overestimated by MCD compared to the observation (harmonic fitting). The seasonal evolution of the cycles are well reflected. The model reveals that semidiurnal tides existed in shaping the spring and autumn diurnal cycle.

deg), Sun-Mars distance $r_{sm}$ (unit: *astronomic unit, AU*) as follows (Zurek et al., 2017):

$$ln(\rho_{mass,150\,km}) = p_1 + p_2\cos(SZA)/r_{sm}^2 + p_3/r_{sm}^2 \quad (5)$$

where $\rho_{mass,150\,km}$ represents normalized density at 150 km. $p_1$, $p_2$, and $p_3$ are parameters. The first term is a constant. The latter two terms represent the flux attenuation from the Sun to Mars and the obliquity evolution of Mars. The model is well fitted with MAVEN data. The model well predicted the harmonic evolution of the upper densities as well as pointed out that the cycle is due to solar heating.

As shown in Figures 5 and 6, and section 3.1.1, the observations have shown that the Martian lower thermosphere is heavily influenced by the surface dust activates, which was firstly observed by MGS (e.g., Keating et al., 1998). The surface dust activities have significant impacts on the Martian thermosphere, especially during autumn and winter, which were observed by density data from all four orbiters. The key role of dust to the Mars atmospheric circulation has been predicted by GCM (e.g., González-Galindo, Forget, Lpez-Valverde, Angelats i Coll, & Millour, 2009; González-Galindo, Forget, Lpez-Valverde, & Angelats i Coll, 2009; Montabone et al., 2015). The rise of the electron density peak of *F1* layer during the dust seasons has been also observed by *Mariner 9* (Fjeldbo & Eshleman, 1968).

Consequently, the annual cycles have variations that are caused by the surface dust activities as shown in Figures 5 and 6. Therefore, the three-parameter model might have difficulty in explaining the comprehensive data of the four orbiters, especially the nonharmonic part during the dust seasons. As a matter of fact, the

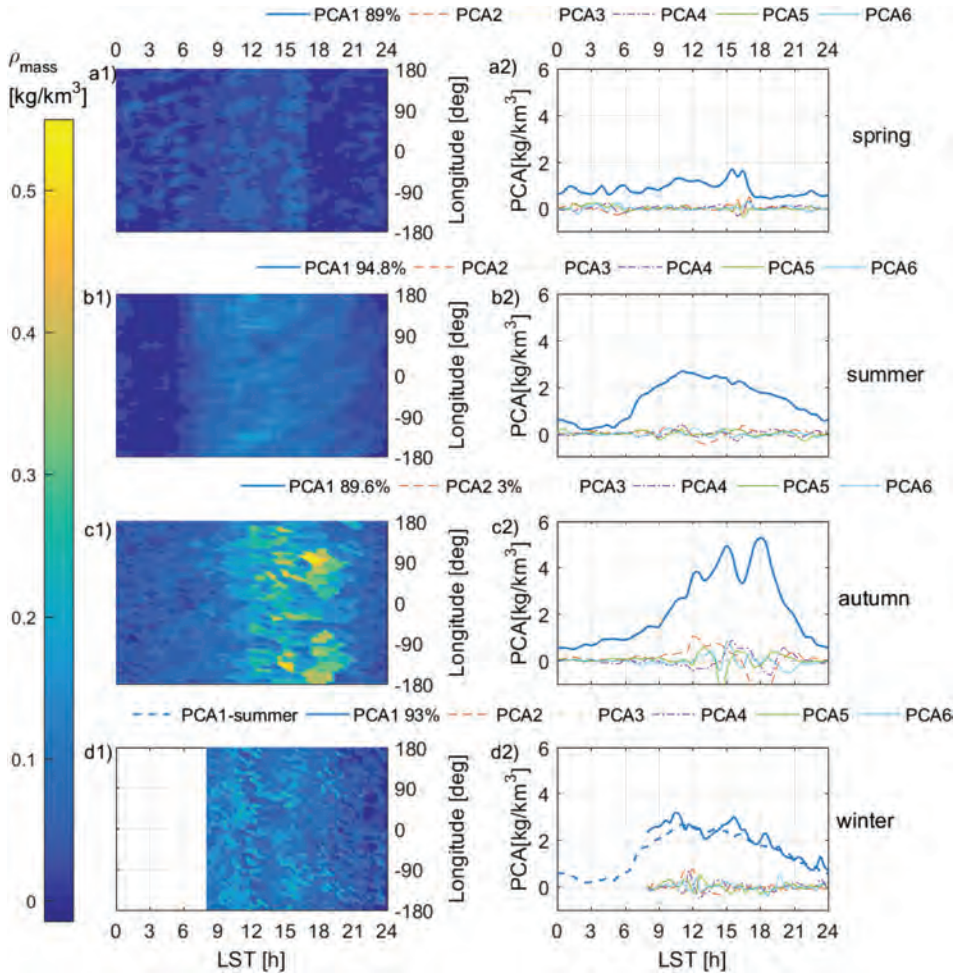


**Figure 3.** Diurnal gravity waves at altitude of 160 km. (left panels) $\rho$ with respect to LST and Longitude. a1 to d1 are interpolations of the original density. (right panels) PCAs. Diurnal cycles dominated (PCA1 > 89%) in all seasons, where both amplitudes and phases have a seasonal evolution from spring to winter. PCA2–6 are less than 3%.

model has distinct biases with the annual cycles of density recovered by MGS, ODY, and MRO in amplitudes. The dust storms have slight impacts on the thermosphere during early summer and vice versa in the other three seasons (Figures 5 and 6). Consequently, we improve the Zurek's model to reasonably explain and fit the annual cycle with considering the dust storm as follows:

$$ln(\rho_{mass,150,km}) = p_1 + p_2\cos(SZA)/r_{sm}^2 + p_3/r_{sm}^2 + p_4 Dust_{IR-CDOD} \quad (6)$$

where $p_4$ is the dust parameters. $Dust_{IR-CDOD}$ is the infrared radiation *CDOD* values to evaluate the dust activities. The model has an advantage to explain the autumn-winter thermospheric density increase.

As illustrated in Figure 7, the MGS/ODY ACC-derived density has rapid rise in dust seasons (Ls 180–360°, e.g., autumn and winter), in which the three-parameter model (Model 1) is not fitted well with the measurements since the perturbations of SZA and $r_{sm}$ are minor during the evolution of Mars. The four-parameter model with the dust term can explain the cycle much more reasonably. The first constant parameter can be regarded as the mean state of the annual density which is generated by the large-scale atmospheric dynamics. The second and third terms are the solar heating effects. The fourth term is the impact of dust activities. As shown in Figures 5–7, the dust activities could change both the amplitude and phase of the density cycles in dust seasons.

Both observations and GCM simulations support that the dust storms have vital impacts on the Mars atmosphere up to the upper layers (e.g., England et al., 2017; Keating et al., 1998; Montabone et al., 2015; Rafkin et al., 2002), which means the dust terms in equation (6) are reasonable. The general impact of the dust

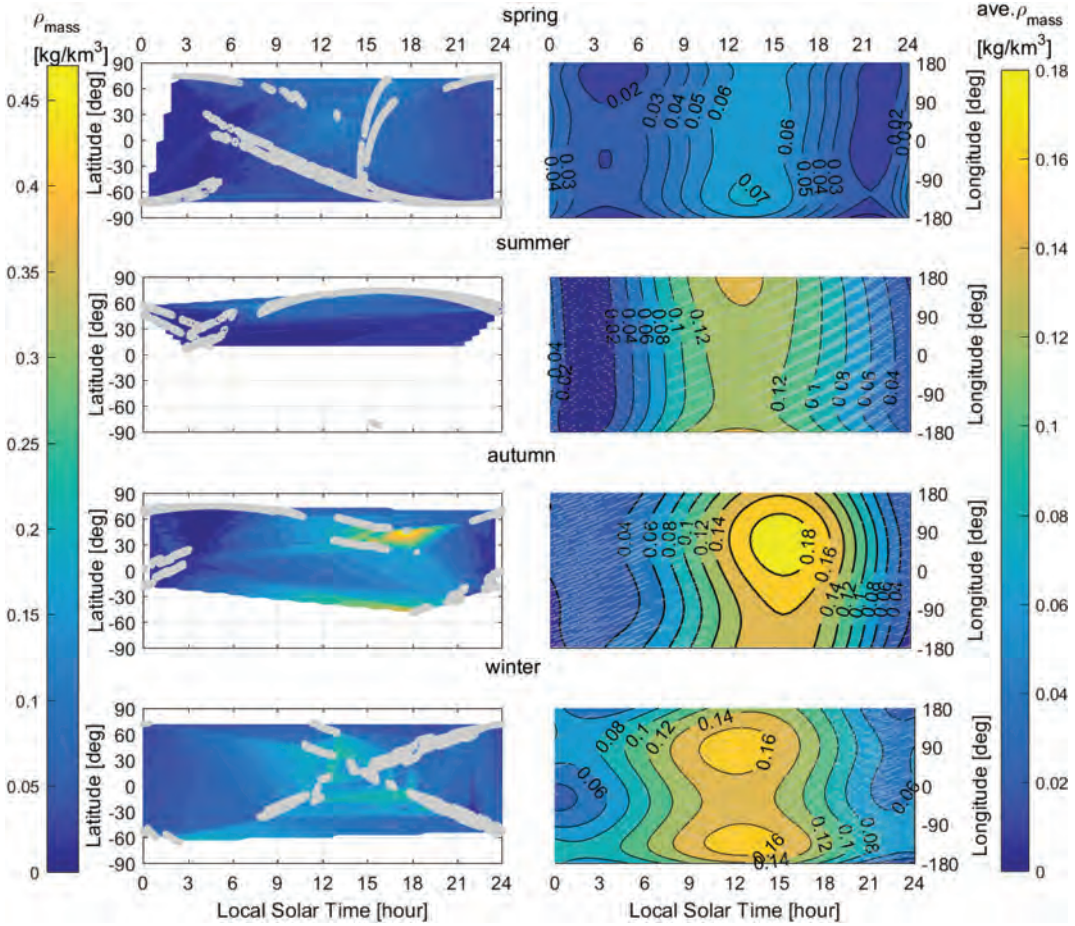


**Figure 4.** (left) Latitude variations of the diurnal cycle by a linear interpolation of the original observations(gray points). The diurnal cycles have latitude-related evolution during the seasonal evolution, which can be predicted by the GCM except that a warming winter equatorial region existed (more explicit latitude distributions are shown in Figure 8). (right) Longitude average by polynomials fitting. The spring longitude measurements (gray points) are too many to be plotted. The reference altitude is 160 km. From top to bottom is spring to winter.

storms on the Mars atmosphere is to expand and lift the atmospheric layers (Smith, 2009). The densities increased during this expansion process. Therefore, the harmonic structure of the annual thermospheric density cycle as well as the seasonal evolution of the diurnal cycle is primarily driven by the seasonal changes (the obliquity orbital evolution of Mars along to the Sun). The amplitude and phase of the cycle are greatly impacted by the presence or absence of lower atmospheric dust storms.

### 3.2. Vertical Variations and Structures

#### 3.2.1. Vertical Structures and Internal Atmospheric Gravity Waves

The vertical structure described by the densities along with the latitude and its PCAs are shown in Figure 8. The vertical densities and corresponding internal atmospheric gravity waves (IAGWs) are illustrated from the top to the bottom panels (spring to winter). The vertical density structures experience an exponential decay with the increasing height and a seasonal evolution of amplitude and global distribution(Figure 8, a2–d2). The polar warming is detectable, which has a seasonal evolution: The densities are higher in NH high and midlatitude region during spring and summer and vice versa during autumn and winter. The phenomenon is caused by the transhemisphere atmospheric circulation that causes the contraction and descent of the polar region parcels (González-Galindo, Forget, Lpez-Valverde, & Angelats i Coll, 2009; Bougher et al., 2006). The structure can be predicted by the GCM. A new phenomenon that should be noticed is that the winter equatorial region has higher density second only to the south polar region. It is illustrated by the MAVEN data and has not been predicted by the GCM. The latitude variations illustrated in Figure 8 are also detected in Figure 4.

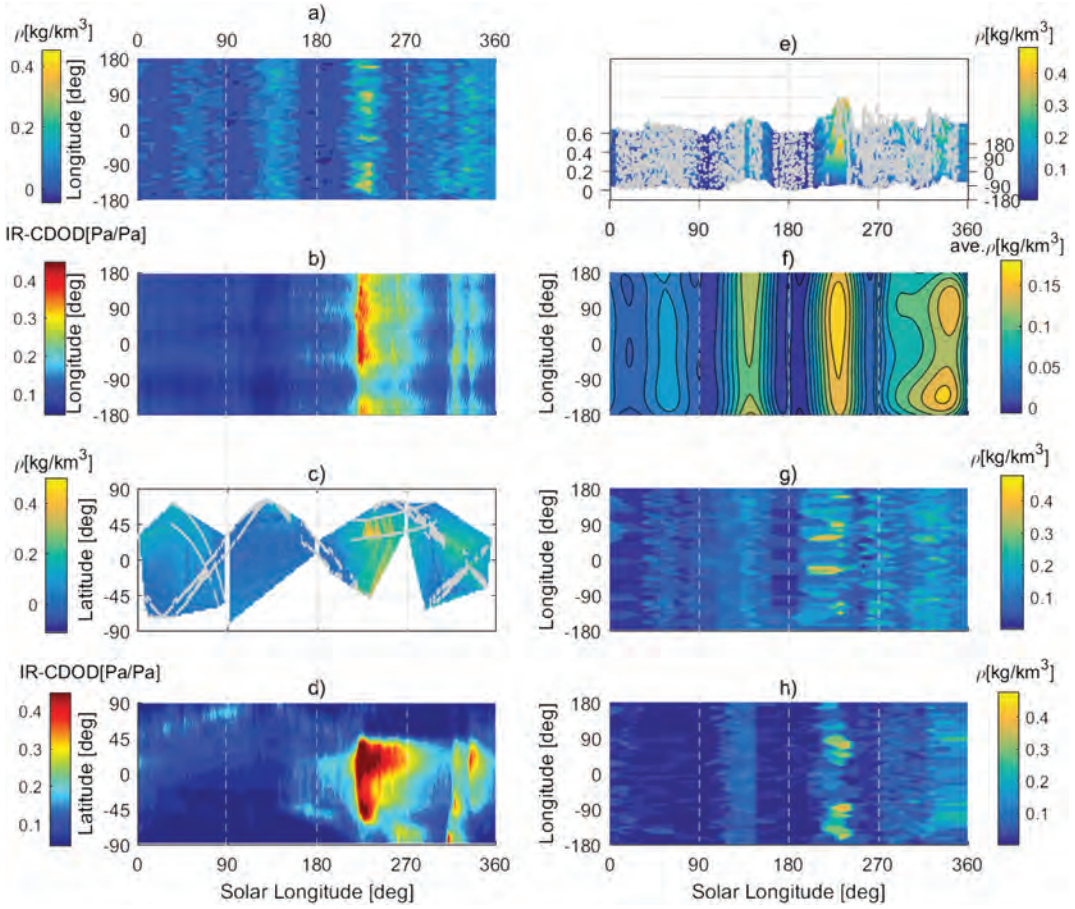


**Figure 5.** The responses of Mars thermospheric density to the surface dust activities at altitude of 160 km. (a) Overall seasonal latitude variation by observations interpolation. (b) Surface dust index IR-CDOD versus longitude. (c) Density versus latitude. (d) IR-CDOD versus latitude. (e) 3-D version of longitude interpolation and densities (gray points). (f) Polynomials fitting at each season to reflect the longitude variations. (g) Dayside density interpolation. (h) Nightside density interpolation. The IR-CDOD (9.3 μm) is from Montabone et al. (2015). The thermospheric densities have strong response to the autumn-winter dust activities.

The relative variations $\Delta\rho/\rho_0$ are shown in Figure 8 (a3–d3). The $\rho_0$ equals the latitude mean of the density. The $\Delta\rho$ is the difference between $\rho_0$ and the density in each latitude. Complex variations are found in all seasons, in which the amplitudes increase with the altitude. The *PCAs* and its harmonic fitting are shown in Figure 8 (a4–d4). The wavelength is between 16 and 20 km. The amplitudes have exponential increase. It is thought to be IAGWs by MAVEN NGIMS data (England et al., 2017). The energy carried by the waves is the key factor that leads to the polar warming (Bougher et al., 2006).

Overall, the seasonal amplitude and phase evolution of the vertical structure of the lower thermosphere are also detectable, where various kinds of IAGWs are existing in the upper layers that have different patterns during the seasonal evolution. The thermospheric density increases distinctly due to the impacts of dust activities during fall and winter. The seasonal polar warming transfer from NH to SH is clear during the evolution.

### 3.2.2. Amplitude Narrowing of IAGWs During Dust Seasons

The vertical waves can be observed by current density data. The relative perturbations $\Delta\rho/\rho_0$ and their PCAs/*EOFs* are shown in Figures 8 and 9. The amplitudes of spring IAGWs exhibit a slow increase from 135 to 185 km. The waves break up where altitude is greater than 190 km. The summer IAGWs rupture and release energies at 185 to 190 km, which is due to the relative lower density distribution during the season. The waves can extend into the exosphere during the dust seasons (autumn and winter, Figure 8, c1–c4).

The surface dust storms are coupled with the IAGWs. The autumn/winter dust activities lift the atmospheric layers, where the IAGWs amplitude is kept similar from 135 to 195 km as shown in Figure 8 (c4–d4) and

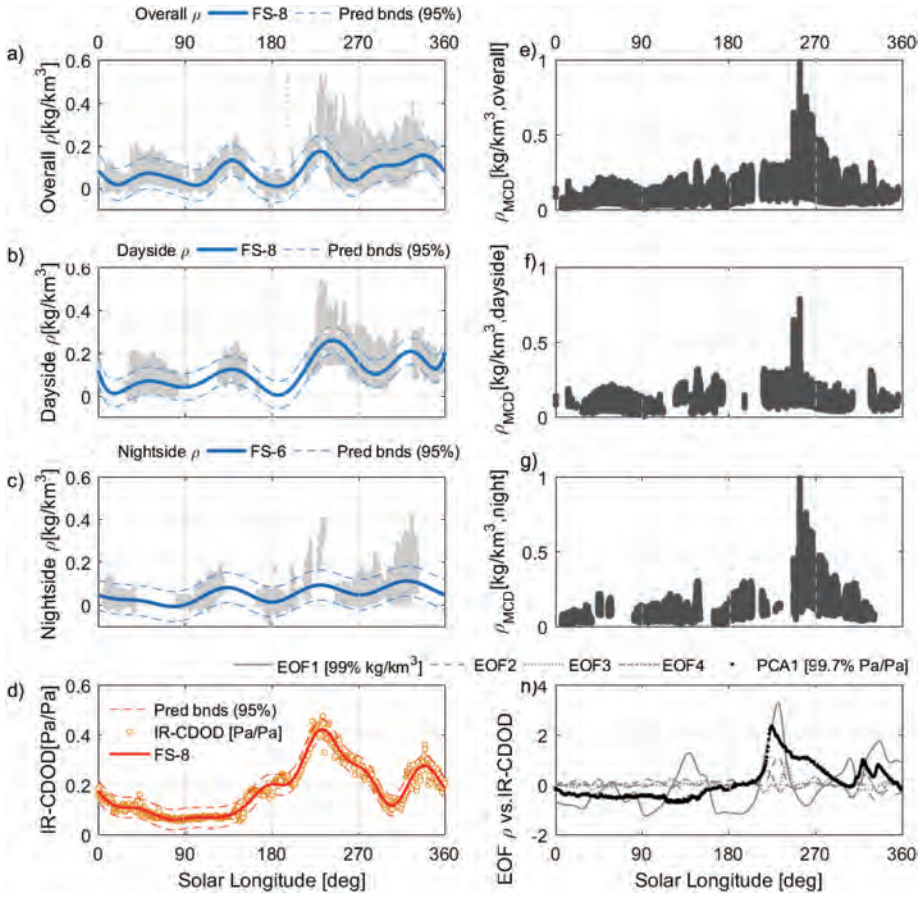


**Figure 6.** Time series of seasonal Mars thermospheric density and IR-CDOD index at altitude of 160 km. (a) seasonal density (overall) variation. (b) Dayside. (c) Nightside. (d) FS fitting with IR-CDOD at equator. (e) Overall $\rho_{MCD}$. (f) Dayside $\rho_{MCD}$. (g) Nightside $\rho_{MCD}$. (h) Principal components of seasonal density versus IR-CDOD. The observations, MCD (MGCM), and the principal components indicate the surface dust storms have vivid impacted effect on the annual thermospheric density cycle.

Figure 9. The results indicate that the IAGWs can extend beyond the exobase without waveform breaking up due to the increased density during the dust seasons, which carry energies of lower layers into the higher layers. The coupling mechanisms between dust activities and IAGWs are as follows: The impacts of the dust storms on the thermosphere can increase the density of the upper layers, which can contain more energies of the waves or increase the altitude of the breaking points of the IAGWs (in this case, the apparent amplitude of the gravity waves at a fixed altitude is diminishing with increased densities). Consequently,the IAGWs or the deposition point of the waves can extend to higher layers even beyond the exobase (200 km). Consequently, the seasonal amplitude evolution of IAGWs is exactly the opposite with the density as shown in sections 3.1.1 and 3.1.2. The dust activities are also triggers of the adjustments of atmospheric parameters under the conservation of the potential temperatures, where the buoyancy force restores the adjustment processes (Fritts & Alexander, 2003; Fritts et al., 2006). The IAGWs have great influence on the wind field, which is one of the important factors that influence the thermospheric structures (England et al., 2017; Terada et al., 2017).

## 4. Discussions

Spring nightside warming and seasonal variations of the diurnal cycles are observed (Figures 1–4). The impacts of the surface dust storms are closely related with the solar radiation to increase the dayside density during the dust seasons. The nightside thermosphere with lower temperature is so thin that the atmosphere cannot be seen as fluid because the volatiles are not well mixed. This could cause wave breaking during

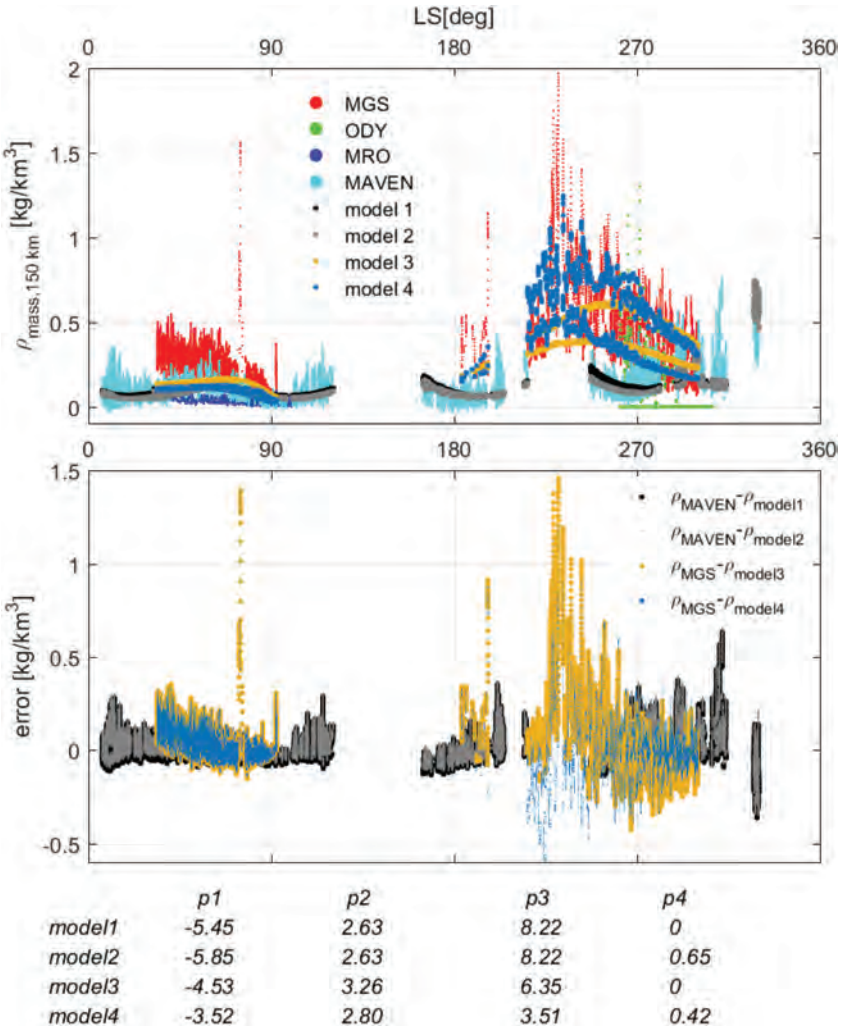


| | p1 | p2 | p3 | p4 |
|---|---|---|---|---|
| model1 | -5.45 | 2.63 | 8.22 | 0 |
| model2 | -5.85 | 2.63 | 8.22 | 0.65 |
| model3 | -4.53 | 3.26 | 6.35 | 0 |
| model4 | -3.52 | 2.80 | 3.51 | 0.42 |

**Figure 7.** Annual density variation and parametrized models at altitude 150 km. Model 1: MAVEN data parametrized by equation (5). Model 2: MAVEN data parametrized by equation (6) using Mars Year (MY32) IR-CDOD values which approximate to mean dust storm condition. Model 3: MGS observations parametrized by equation (5). Model 4: MGS densities parametrized by equation (6) using MY 25 IR-CDOD values which represent global dust storm condition. The IR-CDOD values are from Montabone et al. (2015). Least squares algorithm is used.

the propagation, which includes energy release. The day-night differences and spring night anomalies were noticed by former data (e.g., Forget et al., 2009; Yiğit et al., 2015).

The Martian surface dust activities replace water cycles, compared with the Earth, as the atmospheric reservoirs to transport energy from surface up to 50 km, which is the main general circulation function of Mars (Forget et al., 1999). The dust could change the basic diurnal/seasonal structure of the upper atmosphere as described in this paper (Figures 5 and 6).The transportation functions from 50 km to the upper atmosphere is not well understood. However, the impact of dust storms on the thermosphere have been observed in this paper(Figures 5–7) and other studies (e.g., England et al., 2016; Keating et al., 1998; Rafkin et al., 2002).

The gravity waves generated by the conservation of potential temperature and vorticity are thought to be the key process that transports energies, masses, and momentums from lower layers into upper layers (e.g., Bougher et al., 2017; Forbes et al., 2002; Yiğit et al., 2015). The general altitude of the generators of the IAGWs needs to be fixed to evaluate the magnitude of the waves and the physics. The MGCM simulation to draw deep insight to the physical mechanisms of the gravity waves and their effects on the Martian thermosphere can be seen from previous studies (e.g.,Medvedev & Yiğit, 2012; Medvedev et al., 2011; Yiğit et al., 2008).

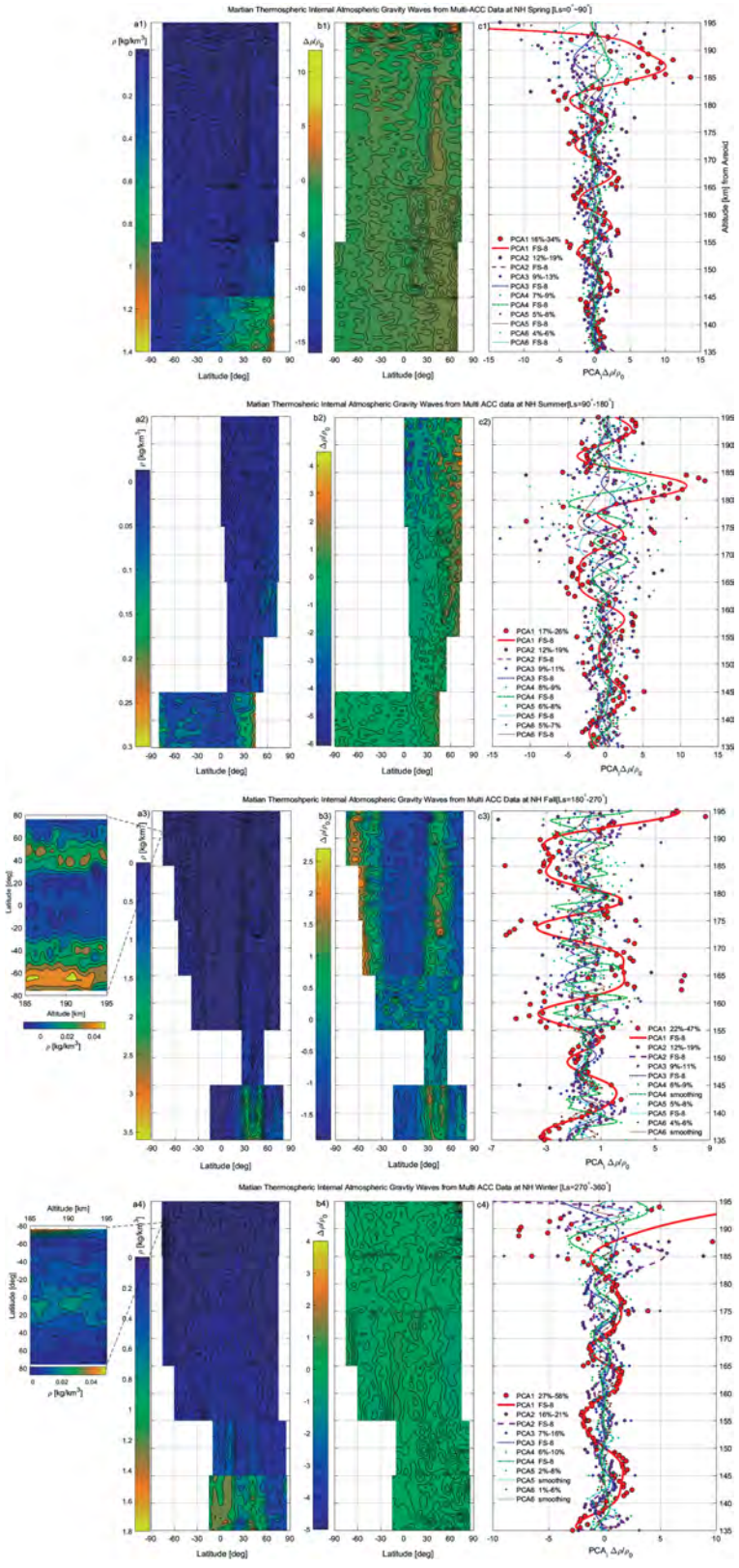


**Figure 8.** Global vertical structure and IAGWs in different seasons. From left to right (1–3): (a) vertical structure retrieved by observations from the four orbiters; (b) relative perturbations $\Delta\rho/\rho_0$; (c) PCAs of (b) and FS fitting. From top to bottom (1–4): spring to winter. A seasonal evolution of the vertical structure is revealed. A winter equatorial warming is reflected by panel a4.

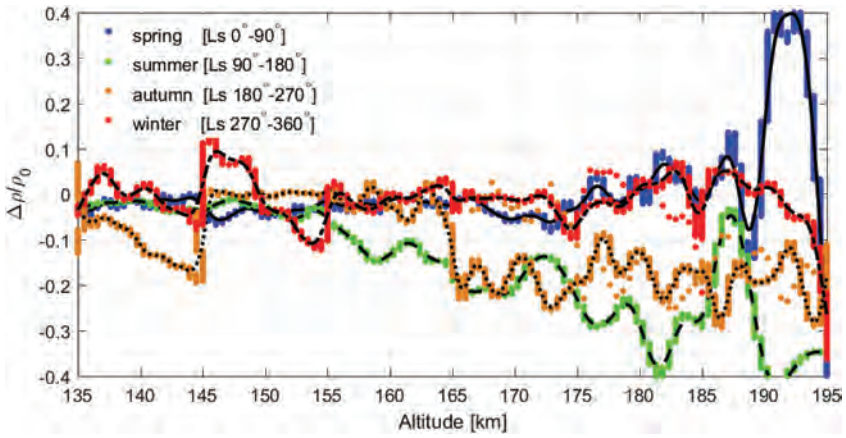


**Figure 9.** Internal atmospheric gravity waves from $\Delta\rho/\rho_0$ in different seasons. The profiles are filtered values of Figure 8 (b1–b4). The autumn and winter perturbations have amplitude within ±10% due to the density expansion during the dust seasons. The summer IAGWs break around 185 km, which has the shortest propagation distance. The amplitude of the IAGWs during autumn/winter are narrower than during spring and summer.

The extents of the gravity waves or the "breaking points" of the waves into the exosphere could cause cooling or heating to the volatiles (Figures 8 and 9), which might influence the structure of the layer and then act on the escape functions. The lower thermospheric IAGW's impact on the wind field of the higher layers is not evaluated. The wind field turbulences can be predicted during the dust seasons where the IAGWs bring more energy into the thermosphere.

The relative perturbations and the waves extracted by PCAs still need to be explained. The waves extracted by the PCA method are not clear due to lack of data, which means the physical processes that control the waves still cannot be revealed. For example, only diurnal cycles can be recognized from the observations (Figure 3).

The ACC densities can reveal much more detailed information than other data sets. The diurnal, seasonal cycles described by the densities are more complete than the occultation data (e.g., Forget et al., 2009; Zurek et al., 2017). It is noticed that the spring, summer, and autumn structure (Figures 4 and 8) can be well predicted by the LMD-GCM. However, the winter has a "warming" equator that is not expected.

## 5. Summaries

The density data from MGS, MRO, ODY, and MAVEN, especially the latter orbiter, are used to investigate the variations of Mars upper atmosphere. The seasonal evolution of the structures and variations of the layer are formatted by solar heating, dust impacts, and relative coupling processes. The diurnal, seasonal/annual, vertical, and global variations are obtained as follows:

The fundamental structure of the cycles are shaped by solar radiation and impacted by dust storms, where the solar heating caused dayside increase of the atmospheric density. The seasonal phase shift of the cycles are due to the obliquity orbital evolution of Mars with respect to the Sun. The dust activities, especially during autumn and winter, can increase the amplitudes with a factor of 1.5 to 2 of the structures as well as change the phase of the cycles. The energy absorption and release process, namely the diurnal "breathes" during different seasons are described and modeled. The spring nightside density increases have been detected. The fast energy absorption and slow release during summer and vice versa in autumn are found. The complex waves are extracted from the data. The solar heating, which is the key process that controls the diurnal density cycles, as well as dust activities, is an important factor in changing the amplitudes and phase of the diurnal and seasonal cycles. A warming (higher density) winter equatorial region is detected in the winter diurnal cycle, which can be observed in all the lower thermosphere.

An improved parametrized model is proposed to fit the seasonal density variations, which is better to explain the data. The former investigations might overstate the dominant roles of solar heating in formatting the thermospheric structures. The dust term has been embedded into the models and accounts for the seasonal

variations, which indicates that the effect of dust on the thermosphere is also an important process for controlling the upper atmosphere.

The upper atmospheric IAGWs, which propagate vertically with increasing amplitudes and negative phase, have been investigated using ACC-derived densities. The IAGWs can extend beyond the exobase during autumn and winter due to the density increase caused by the impacts of the dust storms. The coupling process, where the denser density can contain more energy of the IAGWs and thus restrict the growth of the waves amplitudes or even lift up the wave breaking points, can transport energy, mass, and momentum into higher altitude even beyond the exobase. Consequently, exospheric response to the autumn and winter IAGWs can be expected. The lower vertical amplitude is tightly coincident with the dust activities. Consequently, cooler NH polar and warmer SH polar during the dust seasons can be predicted by this research. The results in this paper, especially the seasonal harmonic evolution of the thermospheric density and the winter equator "warming," can help improving the GCM.

**Acknowledgments**
This work was supported by the High Performance Computing Resource in the Core Facility for Advanced Research Computing at Shanghai Astronomical Observatory. The density data are provided by NASA Planetary Data System (PDS; https://pds-atmospheres.nmsu.edu/data_and_services/atmospheres_data/MARS/mars_orbiter.html). The authors also thank Ehouarn Millour for providing the MGCM. The paper is supported by the Startup Foundation for Introducing Talent of NUIST (Grant 2019r089) and Key Laboratory of Planetary Sciences Project (Grant PSL16_07).

## References

Abdi, H., & Williams, L. J. (2010). Principal component analysis. *Wiley Interdisciplinary Reviews: Computational Statistics*, *2*(4), 433–459. https://doi.org/10.1002/wics.101

Angelats i Coll, M., Forget, F., López-Valverde, M., & González-Galindo, F. (2005). The first Mars thermospheric general circulation model: The Martian atmosphere from the ground to 240 km. *Geophysical Research Letters*, *32*, L04201. https://doi.org/10.1029/2004GL021368

Banfield, D., Conrath, B., Gierasch, P., Wilson, RJohn, & Smith, M. (2004). Traveling waves in the Martian atmosphere from MGS TES nadir data. *Icarus*, *170*(2), 365–403. https://doi.org/10.1016/j.icarus.2004.03.015

Banfield, D., Conrath, B., Smith, M., Christensen, P., & Wilson, R. J. (2003). Forced waves in the Martian atmosphere from MGS TES nadir data. *Icarus*, *161*(2), 319–345. https://doi.org/10.1016/S0019-1035(02)00044-1

Bell, J. M., Bougher, S. W., & Murphy, J. R. (2007). Vertical dust mixing and the interannual variations in the Mars thermosphere. *Journal of Geophysical Research*, *112*, E12002. https://doi.org/10.1029/2006JE002856

Bougher, S., Bell, J., Murphy, J., Lopez-Valverde, M., & Withers, P. (2006). Polar warming in the Mars thermosphere: Seasonal variations owing to changing insolation and dust distributions. *Geophysical Research Letters*, *33*, L02203. https://doi.org/10.1029/2005GL024059

Bougher, S. W., Cravens, TE, Grebowsky, J., & Luhmann, J. (2015). The aeronomy of Mars: Characterization by MAVEN of the upper atmosphere reservoir that regulates volatile escape. *Space Science Reviews*, *195*(1-4), 423–456. https://doi.org/10.1007/s11214-014-0053-7

Bougher, S. W., Jakosky, B., Halekas, J., Grebowsky, J., Luhmann, J., Mahaffy, P., et al. (2015). Early MAVEN deep dip campaign reveals thermosphere and ionosphere variability. *Science*, *350*(6261), aad0459. https://doi.org/10.1126/science.aad0459

Bougher, S., Keating, G., Zurek, R., Murphy, J., Haberle, R., Hollingsworth, J., & Clancy, R. T. (1999). Mars Global Surveyor aerobraking: Atmospheric trends and model interpretation. *Advances in Space Research*, *23*(11), 1887–1897. https://doi.org/10.1016/S0273-1177(99)00272-0

Bougher, S. W., Roeten, K. J., Olsen, K., Mahaffy, P. R., Benna, M., Elrod, M., et al. (2017). The structure and variability of Mars dayside thermosphere from MAVEN NGIMS and IUVS measurements: Seasonal and solar activity trends in scale heights and temperatures. *Journal of Geophysical Research: Space Physics*, *122*, 1296–1313. https://doi.org/10.1002/2016JA023454

Calabia, A., & Jin, S. (2016). New modes and mechanisms of thermospheric mass density variations from GRACE accelerometers. *Journal of Geophysical Research: Space Physics*, *121*, 11,191–11,121. https://doi.org/10.1002/2016JA022594

Creasey, J. E., Forbes, J. M., & Hinson, D. P. (2006). Global and seasonal distribution of gravity wave activity in Mars' lower atmosphere derived from MGS radio occultation data. *Geophysical research letters*, *33*, L01803. https://doi.org/10.1029/2005GL024037

Creasey, J. E., Forbes, J. M., & Keating, G. M. (2006). Density variability at scales typical of gravity waves observed in Mars' thermosphere by the MGS accelerometer. *Geophysical Research Letters*, *33*, L22814. https://doi.org/10.1029/2006GL027583

Di Achille, G., & Hynek, B. M. (2010). Ancient ocean on Mars supported by global distribution of deltas and valleys. *Nature Geoscience*, *3*(7), 459–463. https://doi.org/10.1038/ngeo891

England, S. L., Liu, G., Withers, P., Yiğit, E., Lo, D., Jain, S., et al. (2016). Simultaneous observations of atmospheric tides from combined in situ and remote observations at Mars from the MAVEN spacecraft. *Journal of Geophysical Research: Planets*, *121*, 594–607. https://doi.org/10.1002/2016JE004997

England, S. L., Liu, G., Yiğit, E, Mahaffy, P., Elrod, M., Benna, M., et al. (2017). Maven NGIMS observations of atmospheric gravity waves in the Martian thermosphere. *Journal of Geophysical Research: Space Physics*, *122*, 2310–2335. https://doi.org/10.1002/2016JA023475

Fjeldbo, G., & Eshleman, V. R. (1968). The atmosphere of Mars analyzed by integral inversion of the Mariner IV occultation data. *Planetary and Space Science*, *16*(8), 1035–1059. https://doi.org/10.1016/0032-0633(68)90020-2

Forbes, J. M., Bridger, A. F., Bougher, S. W., Hagan, M. E., Hollingsworth, J. L., Keating, G. M., & Murphy, J. (2002). Nonmigrating tides in the thermosphere of Mars. *Journal of Geophysical Research*, *107*(E11), 5113. https://doi.org/10.1029/2001JE001582

Forget, F. (2013). On the probability of habitable planets. *International Journal of Astrobiology*, *12*(3), 177–185. https://doi.org/10.1017/S1473550413000128

Forget, F., Hourdin, F., Fournier, R., Hourdin, C., Talagrand, O., Collins, M., et al. (1999). Improved general circulation models of the Martian atmosphere from the surface to above 80 km. *Journal of Geophysical Research*, *104*(E10), 24,155–24,175. https://doi.org/10.1029/1999JE001025

Forget, F., Montmessin, F., Bertaux, J.-L., González-Galindo, F., Lebonnois, S., Quemerais, E., et al. (2009). Density and temperatures of the upper Martian atmosphere measured by stellar occultations with Mars Express SPICAM. *Journal of Geophysical Research*, *114*, E01004. https://doi.org/10.1029/2008JE003086

Fritts, D. C., & Alexander, M. J. (2003). Gravity wave dynamics and effects in the middle atmosphere. *Reviews of Geophysics*, *41*(1), 1003. https://doi.org/10.1029/2001RG000106

Fritts, D. C., Wang, L., & Tolson, R. H. (2006). Mean and gravity wave structures and variability in the Mars upper atmosphere inferred from Mars Global Surveyor and Mars Odyssey aerobraking densities. *Journal of Geophysical Research*, *111*, A12304. https://doi.org/10.1029/2006JA011897

González-Galindo, F, Forget, F., López-Valverde, M., & Angelats i Coll, M. (2009). A ground-to-exosphere Martian general circulation model: 2. Atmosphere during solstice conditions-thermospheric polar warming. *Journal of Geophysical Research*, *114*, E08004. https://doi.org/10.1029/2008JE003277

González-Galindo, F, Forget, F., López-Valverde, M., Angelats i Coll, M., & Millour, E. (2009). A ground-to-exosphere Martian general circulation model: 1. Seasonal, diurnal, and solar cycle variation of thermospheric temperatures. *Journal of Geophysical Research*, *114*, E04001. https://doi.org/10.1029/2008JE003246

Jakosky, B. M., Grebowsky, J. M., Luhmann, J. G., Connerney, J., Eparvier, F., Ergun, R., et al. (2015). MAVEN observations of the response of Mars to an interplanetary coronal mass ejection. *Science*, *350*(6261), aad0210. https://doi.org/10.1126/science.aad0210

Jakosky, B. M., Lin, RP, Grebowsky, J., Luhmann, J., Mitchell, D., Beutelschies, G., et al. (2015). The Mars Atmosphere and Volatile Evolution (MAVEN) mission. *Space Science Reviews*, *195*(1-4), 3–48. https://doi.org/10.1007/s11214-015-0139-x

Jakosky, B. M., & Phillips, R. J. (2001). Mars' volatile and climate history. *nature*, *412*(6843), 237–244. https://doi.org/10.1038/35084184

Jakosky, B. M., Slipski, M., Benna, M., Mahaffy, P., Elrod, M., Yelle, R., et al. (2017). Mars atmospheric history derived from upper-atmosphere measurements of 38Ar/36Ar. *Science*, *355*(6332), 1408–1410. https://doi.org/10.1126/science.aai7721

Jin, S. G., Calabia, A., & Yuan, L. (2018). Thermospheric variations from GNSS and accelerometer measurements on small satellites. *Proc. IEEE*, *106*(3), 484–495. https://doi.org/10.1109/JPROC.2018.2796084

Keating, G., Bougher, S., & Tolson, R. (2008). Properties of the Mars upper atmosphere derived from accelerometer measurements, *37th COSPAR Scientific Assembly* (pp. 1478). Montreal, Canada.

Keating, G., Bougher, S., Zurek, R., Tolson, R., Cancro, G., Noll, S., et al. (1998). The structure of the upper atmosphere of Mars: In situ accelerometer measurements from Mars Global Surveyor. *Science*, *279*(5357), 1672–1676. https://doi.org/10.1126/science.279.5357.1672

Kliore, A. J., Cain, D. L., Fjeldbo, G., Seidel, B. L., Sykes, M. J., & Rasool, S. (1972). The atmosphere of Mars from Mariner 9 radio occultation measurements. *Icarus*, *17*(2), 484–516. https://doi.org/10.1016/0019-1035(72)90014-0

Liu, J., Richardson, M. I., & Wilson, R. J. (2003). An assessment of the global, seasonal, and interannual spacecraft record of Martian climate in the thermal infrared. *Journal of Geophysical Research*, *108*(E8), 5089. https://doi.org/10.1029/2002JE001921

Mahaffy, P. R., Webster, C. R., Atreya, S. K., Franz, H., Wong, M., Conrad, P. G., et al. (2013). Abundance and isotopic composition of gases in the Martian atmosphere from the Curiosity Rover. *Science*, *341*(6143), 263–266. https://doi.org/10.1126/science.1237966

Medvedev, A. S., & Yiğit, E. (2012). Thermal effects of internal gravity waves in the Martian upper atmosphere. *Geophysical Research Letters*, *39*, L05201. https://doi.org/10.1029/2012GL050852

Medvedev, A. S., Yiğit, E., Hartogh, P., & Becker, E. (2011). Influence of gravity waves on the Martian atmosphere: General circulation modeling. *Journal of Geophysical Research*, *116*, E1000. https://doi.org/10.1029/2011JE003848

Millour, E., Forget, F., Spiga, A., Navarro, T., Madeleine, J.-B., Montabone, L., et al. (2015). The Mars Climate Database (MCD version 5.2). In *European planetary science congress*.

Montabone, L., Forget, F., Millour, E., Wilson, R., Lewis, S., Cantor, B., et al. (2015). Eight-year climatology of dust optical depth on Mars. *Icarus*, *251*, 65–95. https://doi.org/10.1016/j.icarus.2014.12.034

Nier, A., & McElroy, M. B. (1977). Composition and structure of Mars' upper atmosphere: Results from the neutral mass spectrometers on Viking 1 and 2. *Journal of Geophysical Research*, *82*(28), 4341–4349. https://doi.org/10.1029/JS082i028p04341

Rafkin, S. C., Maria, M. R. S., & Michaels, T. I. (2002). Simulation of the atmospheric thermal circulation of a Martian volcano using a mesoscale numerical model. *Nature*, *419*(6908), 697–669. https://doi.org/10.1038/nature01114

Seiff, A., & Kirk, D. B. (1977). Structure of the atmosphere of Mars in summer at mid-latitudes. *Journal of Geophysical Research*, *82*, 4364–4378. https://doi.org/10.1029/JS082i028p04364

Smith, M. D. (2009). Themis observations of Mars aerosol optical depth from 2002–2008. *Icarus*, *202*(2), 444–452. https://doi.org/10.1016/j.icarus.2009.03.027

Terada, N., Leblanc, F., Nakagawa, H., Medvedev, A. S., Yiğit, E., Kuroda, T., et al. (2017). Global distribution and parameter dependences of gravity wave activity in the Martian upper thermosphere derived from MAVEN/NGIMS observations. *Journal of Geophysical Research: Space Physics*, *122*, 2374–2397. https://doi.org/10.1002/2016JA023476

Tolson, R. H., Bemis, E., Zaleski, K., Keating, G., Shidner, J. D., Brown, S., et al. (2008). Atmospheric modeling using accelerometer data during Mars reconnaissance orbiter aerobraking operations. *Journal of Spacecraft and Rockets*, *45*(3), 511–518.

Tolson, R. H., Dwyer, A., Hanna, J., Keating, G., George, B., Escalera, P., & Werner, M. (2005). Application of accelerometer data to Mars Odyssey aerobraking and atmospheric modeling. *Journal of Spacecraft and Rockets*, *42*(3), 435–443.

Tolson, R. H., Keating, G., Zurek, R., Bougher, S., Justus, C., & Fritts, D. (2007). Application of acclerometer data to atmospheric modeling during Mars aerobraking operations. *Journal of Spacecraft and Rockets*, *44*(6), 1172–1179.

Wang, L., Fritts, D., & Tolson, R. (2006). Nonmigrating tides inferred from the Mars Odyssey and Mars Global Surveyor aerobraking data. *Geophysical research letters*, *33*, L23201. https://doi.org/10.1029/2006GL027753

Wilson, R. J. (2002). Evidence for nonmigrating thermal tides in the Mars upper atmosphere from the Mars Global Surveyor accelerometer experiment. *Geophysical Research Letters*, *29*(7), 1120. https://doi.org/10.1029/2001GL013975

Withers, P., Bougher, S., & Keating, G. (2003). The effects of topographically-controlled thermal tides in the Martian upper atmosphere as seen by the MGS accelerometer. *Icarus*, *164*(1), 14–32. https://doi.org/10.1016/S0019-1035(03)00135-0

Yiğit, E., Aylward, A. D., & Medvedev, A. S. (2008). Parameterization of the effects of vertically propagating gravity waves for thermosphere general circulation models: Sensitivity study. *Journal of Geophysical Research*, *113*, D19106. https://doi.org/10.1029/2008JD010135

Yiğit, E., England, S. L., Liu, G., Medvedev, A. S., Mahaffy, P. R., Kuroda, T., & Jakosky, B. M. (2015). High-altitude gravity waves in the Martian thermosphere observed by MAVEN/NGIMS and modeled by a gravity wave scheme. *Geophysical Research Letters*, *42*, 8993–9000. https://doi.org/10.1002/2015GL065307

Zurek, R. W., & Leovy, C. (1981). Thermal tides in the dusty Martian atmosphere: A verification of theory. *Science*, *213*(4506), 437–439. https://doi.org/10.1126/science.213.4506.437

Zurek, R. W., Tolson, R. H., Baird, D., Johnson, M. Z., & Bougher, S. W. (2015). Application of MAVEN accelerometer and attitude control data to Mars atmospheric characterization. *Space Science Reviews*, *195*(1-4), 303–317. https://doi.org/10.1007/s11214-014-0095-x

Zurek, R. W., Tolson, R., Bougher, S., Lugo, R., Baird, D., Bell, J., & Jakosky, B. (2017). Mars thermosphere as seen in MAVEN accelerometer data. *Journal of Geophysical Research: Space Physics*, *122*, 3798–3814. https://doi.org/10.1002/2016JA023641